metals

MDPI

Article

The Determination of the Elastoplastic and Phase-Field Parameters for Monotonic and Fatigue Fracture of Sintered Steel Astaloy™ Mo+0.2C

Tomislav Polančec *, Tomislav Lesičar and Zdenko Tonković

Laboratory of Numerical Mechanics, Faculty of Mechanical Engineering and Naval Architecture, Ivana Lučića 5, 10000 Zagreb, Croatia; tomislav.lesicar@fsb.unizg.hr (T.L.); zdenko.tonkovic@fsb.unizg.hr (Z.T.)
* Correspondence: tomislav.polancec@fsb.unizg.hr

Abstract: This paper presents a procedure for determining the elastoplastic parameters of phase-field fracture of sintered material. The material considered was sintered steel Astaloy™ Mo+0.2C of three densities: 6.5, 6.8 and 7.1 g/cm^3. The stress–strain curve and Wöhler curve, which are experimentally obtained, are utilized for validation of the numerical simulations. For modelling of damage evolution, a CCPF (Convergence check phase-field) algorithm was used as a numerical framework. During calibration of the numerical parameters, two-dimensional as well as three-dimensional modelling was used. A comparison of different fatigue degradation functions known from the literature is also made. To improve the efficiency of numerical simulations of fatigue behaviour, the cycle skip technique is also employed.

Keywords: phase-field; fatigue; sintered steel; numerical modelling

check for updates

Citation: Polančec, T.; Lesičar, T.; Tonković, Z. The Determination of the Elastoplastic and Phase-Field Parameters for Monotonic and Fatigue Fracture of Sintered Steel Astaloy™ Mo+0.2C. *Metals* **2024**, *14*, 1138. https://doi.org/10.3390/met14101138

Academic Editor: Fabio Scherillo

Received: 29 August 2024
Revised: 1 October 2024
Accepted: 3 October 2024
Published: 5 October 2024

Copyright: © 2024 by the authors. Licensee MDPI, Basel, Switzerland. This article is an open access article distributed under the terms and conditions of the Creative Commons Attribution (CC BY) license (https://creativecommons.org/licenses/by/4.0/).

1. Introduction

This paper is a continuation of the authors' previous research on sintered steel Astaloy™ Mo+0.2C [1,2]. In contrast to costly, unfeasible or challenging experiments, numerical modelling of fracture emerges as a more viable solution. Recently, the phase-field method has garnered substantial attention within the scientific community for modelling of fracture occurrences. In physics, phase-field fracture models were built on the Ginzburg-Landau theory [3], while in mechanics, these models utilize Griffith's theory [4] as a foundation. Francfort and Marigo [5] generalized the fracture criterion, advancing toward phase-field fracture modelling. This methodology relies on total energy minimization, encompassing both fracture and elastic energy, enabling predictions of crack initiation and the development of complex crack patterns. Bourdin [6] regularized the variational formulation, facilitating crack evolution determination and numerical integration. The phase-field method has been proven as effective in solving various fracture processes like crack initiation, propagation, merging, kinking and branching, but to capture high gradients of phase-field variable accurately, a fine mesh in the diffuse crack region is essential. Significant advancements in modelling quasi-static brittle fracture have been made by Miehe et al. [7], while Ambati et al. [8] provided a concise summary of phase-field brittle fracture. Numerous recent publications have expanded the phase-field application to brittle fracture [9–11] and extended its abilities toward ductile damage of solids [12]. The research areas proposed include the phase-field method considering small strain [13], as well as the large strain assumption [14]. Recently, significant research efforts within the phase-field framework have been directed towards extending its application to fatigue studies. Amendola [15] as well as Caputo and Fabrizio [16] adopted the Ginzburg-Landau form, considering fatigue potential as a measure of material degradation and softening during cyclic loading. Carrara et al. [17], Alessi et al. [18], and Seiler et al. [19] proposed incorporating degradation fracture energy based on stress or strain history. Notably, the

previously presented research in the phase-field fatigue field assumes linear elastic material behaviour. However, Ulloa et al. [20] expanded the phase-field fatigue model by considering elastoplastic material behaviour, unlike the preceding research efforts. In contrast, Seleš et al. [21] introduced a phase-field fatigue numerical framework applicable to both high-cycle and low-cycle regimes. Khalil et al. [22] considered comparing different fatigue degradation functions, including asymptotic and logarithmic approaches. One of the major challenges in the numerical application of the currently proposed phase-field models is their robustness. The phase-field numerical framework can be devised in a monolithic or staggered manner. The monolithic approach computes phase-field variable and displacements simultaneously. However, a significant disadvantage is the instability during critical crack propagation due to the non-convexity of the regularized free energy functional concerning displacement and phase-field parameters [9]. On the other hand, the staggered scheme calculates phase-field variable and displacements separately, reinstating convexity in the underlying free energy functional. This method splits the weak formulation into two equations using a split operator, enabling an iterative solution. Miehe et al. proposed a single iteration staggered procedure [7], but this approach is computationally demanding and expensive due to the requirement for small loading increments. To address this, Bourdain et al. [23] and Duda et al. [24] tackled the issue of small loading increments by integrating more iterations during a single loading increment, constrained by a stopping criterion. Additionally, in [25], gradual convergence rate issues were bypassed by involving over-relaxed alternate minimization with Newton-type methods [26].

The various examples are presented in the literature for validation of monotonic and cyclic loading by phase-field method for different materials. Ambati et al. [27] validated the phase-field and elastoplastic material parameters from the force-displacement diagrams for Al-5005 and steel-1.0553 by a staggered solution algorithm. The force-displacement diagrams are obtained from uniaxial tensile tests of specimens. Nagaraja et al. [28] provided the validated phase-field parameters of anisotropic brittle fracture in silicon, while Mattey et al. [29] presented the validated parameters for 3D-printed thermoplastics and composites. In [29], the staggered solution algorithm is adopted for thermoplastic, while for composites, the monolithic scheme is used. The phase-field is also used in biomechanics, where in [30], Hug et al. used the phase-field method to describe damage in the proximal humerus by a staggered solution scheme. Except validation of the phase-field and material parameters during monotonic loading, all the mentioned parameters are validated in the literature by introducing fatigue degradation functions. Seleš et al. [21] extended the validation of the phase-field parameters on the fatigue problems by a staggered solution scheme algorithm through introducing validated fatigue degradation functions for nodular cast iron. On the other hand, Haveroth et al. [31] validated the fatigue parameters on the 7075-T7351 aluminium alloy by using a return mapping algorithm, which belongs to a monolithic scheme, with exponent, cubic and combined degradation functions. The numerical framework which has been proven to be suitable and fast for describing the brittle, ductile as well as fatigue fracture is a Convergence Check Phase Field (CCPF) algorithm derived in [32]. Therefore, in this paper, CCPF is utilized for numerical modelling of constitutive and fatigue behaviour of sintered steel Astaloy™ Mo+0.2C. By comparing the results of numerical simulations to the experimental testing, the parameters of elastoplastic material behaviour, like quasi-brittle and fatigue fracture, have been determined.

The paper is organized as follows. In Section 2, the governing equations of the phase-field method along with constitutive modelling of material are explained. Comments on implementation into finite element method are given. Section 3 presents numerical validation of material and phase-field parameters during monotonic loading, while Section 4 deals with numerical validation of Wöhler's curve and determination of phase-field fatigue parameters. Section 5 gives some conclusion remarks and plan of future investigation.

2. Phase-Field Method

In this section, the theoretical foundation of the phase-field method (PF) is presented, utilized for modelling material fatigue and damage. Originating from Griffith's theory [4], the PF method proves to be a practical approach for delineating materials through a seamless transition from undamaged to fully damaged state by incorporating phase-field variable ϕ [23]. The diffusive band width is governed by the length scale parameter l. Notably, the PF method sidesteps the complexities associated with a priori unknown crack paths by eliminating the need for ad hoc criteria in its formulation. In the context of the current research involving sintered steel, elastoplastic material behaviour is adopted, assuming isothermal conditions and adhering to small strain theory. Since sintered steel is characterized by quasi-brittle behaviour, PF methodology incorporating ductility and threshold PF model is pertinent here [21]. Furthermore, in the context of repetitive loading, an extension of the PF method encompassing fatigue is acknowledged [21]. Consequently, the phase-field framework utilized herein relies on the minimization of the internal energy potential for a body [21]:

$$\Psi\left(\varepsilon^{e}, \varepsilon^{p}, \phi, \overline{\psi}\right) = \int_{\Omega} \left\{ g(\phi)\left[\psi_{e}^{+}(\varepsilon^{e}) + \psi_{p}(\varepsilon^{p})\right] + \psi_{e}^{-}(\varepsilon^{e}) \right\} d\Omega \; + \; \int_{\Omega} \hat{F}\left(\overline{\psi}\right) \psi_{c} \left[2\phi + l|\nabla\phi|^{2} \right] d\Omega, \tag{1}$$

where ε^{e} displays elastic strain tensor and ε^{p} represents the plastic strain tensor. Additionally, the reduction in material stiffness after damage initiation is incorporated through a quadratic degradation function:

$$g(\phi) = (1-\phi)^{2} \tag{2}$$

where ψ_{c} represents an energetic threshold required to generate new crack surfaces. By knowing stress–strain or force-displacement diagrams of a material, its energetic threshold can be easily determined by integrating the area below the curve. However, if material degradation emerges in the early stage of the loading, the threshold model might not be suitable for modelling of damage phenomena. Instead, other PF models should be used [8]. To prevent unrealistic crack propagation under compressive conditions, it is essential to decompose the elastic strain energy density into positive (ψ_{e}^{+}) and negative (ψ_{e}^{-}) components [21]. The material considered does not have the ability to heal, so the condition of irreversibility can be established by introducing the parameter of history $\mathcal{H}$. Moreover, this study adopts the volumetric-deviatoric decomposition proposed by Amor [33], although alternative decomposition approaches are available in the literature [34]. By considering the variation of internal energy, quasi-static equilibrium and applying the virtual work principle, the strong form of the equation is derived [21]:

$$\begin{gathered} \nabla \cdot \boldsymbol{\sigma} + \overline{\mathbf{b}} = \mathbf{0} \text{ in } \Omega, \\ \boldsymbol{\sigma} \cdot \mathbf{n} = \overline{\mathbf{t}} \text{ on } \partial\Omega_{\overline{t}}, \\ \mathbf{u} = \overline{\mathbf{u}} \text{ on } \partial\Omega_{\overline{u}}, \\ -l^{2}\Delta\phi + [1+\mathcal{H}]\phi = \mathcal{H} \text{ in } \Omega, \\ \nabla\phi \cdot \mathbf{n} = 0 \text{ on } \partial\Omega, \end{gathered} \tag{3}$$

where $\overline{\mathbf{b}}$ represents the volume force vector, $\overline{\mathbf{t}}$ is the surface force vector, $\overline{\mathbf{u}}$ represents the displacement vector, $\mathbf{n}$ is the outward-pointing normal vector and $\boldsymbol{\sigma}$ denotes the Cauchy stress tensor. More details on derivation of the governing set of equations in phase-field can be found in [21].

Moreover, material fatigue degradation is integrated into the energy potential [21] through the fatigue degradation function $\hat{F}\left(\overline{\psi}\right)$, depending on the local accumulation variable $\overline{\psi}(t)$. It is imperative that $\overline{\psi}(t)$ does not influence monotonic loading cases. Thus, $\overline{\psi}(t)$ is characterized as the sum of negative differences during cyclic loading, implying an increase of $\overline{\psi}(t)$ during the unloading. The local accumulation variable can be described in integral form as follows:

$$\overline{\psi}(t) = \int_0^t \psi_e(t) H\left(-\dot{\psi}_e\right) dt, \tag{4}$$

where H is the following Heaviside function:

$$\begin{aligned} H\left(-\dot{\psi}_e\right) &= 1; \quad \dot{\psi}_e > 0, \\ H\left(-\dot{\psi}_e\right) &= 0; \quad \dot{\psi}_e \leq 0. \end{aligned} \tag{5}$$

The fatigue degradation function actively reduces the range of the load amplitudes within which crack initiation and propagation occurs during cyclic loading by diminishing the energetic barrier required for damage initiation, as shown in Equation (1). In this paper, three fatigue degradation functions also known from literature are presented and validated [21]:

$$\begin{aligned} F_1(\overline{\psi}) &= \left(1 - \frac{\overline{\psi}}{\overline{\psi}+\overline{\psi}_\infty}\right)^2 \text{ for } \overline{\psi} \in [0, +\infty], \\ F_2(\overline{\psi}) &= \left(1 - \frac{\overline{\psi}}{\overline{\psi}_\infty}\right)^2 \text{ for } \overline{\psi} \in [0, \overline{\psi}_\infty], \\ F_3(\overline{\psi}) &= \left(\log \frac{\overline{\psi}_\infty}{\overline{\psi}}\right)^2 \text{ for } \overline{\psi} \in [\overline{\psi}_\infty, 10 \cdot \overline{\psi}_\infty]. \end{aligned} \tag{6}$$

$\overline{\psi}_\infty$ denotes a material-dependant fatigue parameter.

Since in sintered steel investigated herein plastic deformation and strain hardening occur prior to the material fracture, von Mises yield criterion is employed, incorporating nonlinear isotropic and kinematic hardening. The governing constitutive laws are presented here for completeness. The potential of plastic energy dissipation required for driving of PF can be expressed as follows:

$$\psi^P(\varepsilon^P) = \int_0^t (\mathrm{dev}[\sigma^*] - \boldsymbol{\alpha}) : \dot{\varepsilon}^P \, dt, \tag{7}$$

where σ^* denotes the effective Cauchy stress tensor, while $\boldsymbol{\alpha}$ is the backstress tensor. The progression rule for nonlinear kinematic hardening is chosen according to [35]:

$$\dot{\boldsymbol{\alpha}}_k = C_k \frac{1}{\sigma_y\left(\varepsilon^P_{eqv}\right)} (\sigma^* - \boldsymbol{\alpha}) \dot{\varepsilon}^P{}_{eqv} - \gamma_k \boldsymbol{\alpha}_k \dot{\varepsilon}^P{}_{eqv}. \tag{8}$$

The backstress tensor $\boldsymbol{\alpha}_k$ is determined by material parameters γ_k and C_k. The complete backstress tensor is acquired through $\boldsymbol{\alpha} = \Sigma_k \boldsymbol{\alpha}_k$. In this paper, a single backstress tensor is utilized (k = 1). Furthermore, the isotropic hardening law used was the Voce equation [35]:

$$\sigma_y\left(\varepsilon^P_{eqv}\right) = \sigma_y^0 + Q_\infty \left(1 - \exp\left(-b\varepsilon^P_{eqv}\right)\right) \tag{9}$$

σ_y^0 denotes the elasticity limit, while b and Q_∞ ($Q\infty$ is the stress saturation for the current yield stress) are the material parameters. The calibration of material parameters of elastoplasticity is discussed thoroughly in Section 3.

For implementation of the described phase-field methodology into a finite element framework, the Convergence-Check Phase-Field (CCPF) staggered solution scheme suggested by Lesičar et al. [32] is employed. The algorithm necessitates two mesh layers, with one special-purpose finite element in the third layer designated for implementing the stopping criterion and controlling of the variable exchange among layers. The algorithm is incorporated into the finite element software ABAQUS (version 6.21) [36] using user subroutines. The first layer, consisting of structural finite elements, utilizes the user material subroutine UMAT, while the second layer is discretized by the phase field elements through the UEL subroutine. The residual force vectors of displacement field and phase field, respectively, are:

$$\begin{aligned} \mathbf{R}^{\mathbf{v}} &= \int_{\Omega} \mathbf{N}^{\mathrm{v}} \overline{\mathbf{b}} \mathrm{d}\Omega - \int_{\Omega} \mathbf{B}^{\mathrm{v}^T} \boldsymbol{\sigma} \mathrm{d}\Omega, \\ \mathbf{R}^{\phi} &= -\int_{\Omega} \left\{ l^2 \mathbf{B}^{\phi^T} \mathbf{B}^{\phi} \phi + \left[(1+\mathcal{H}) \mathbf{N}^{\phi} \phi - \mathcal{H} \right] \mathbf{N}^{\phi} \right\} \mathrm{d}\Omega, \end{aligned} \tag{10}$$

where **N** represents shape function matrix, while **B** represents the spatial derivative matrix. The stiffness matrices of the structural and PF finite elements, respectively, are as follows:

$$\begin{aligned} \mathbf{K}^{\mathbf{vv}} &= -\frac{\partial \mathbf{R}^{\mathbf{v}}}{\partial \mathbf{v}} = \int_{\Omega} \mathbf{B}^{\mathrm{v}^{\mathrm{T}}} \mathbf{C} \mathbf{B}^{\mathbf{v}} \mathrm{d}\Omega, \\ \mathbf{K}^{\phi\phi} &= -\frac{\partial \mathbf{R}^{\phi}}{\partial \phi} = \int_{\Omega} \left\{ l^2 \mathbf{B}^{\phi^T} \mathbf{B}^{\phi} + [1+\mathcal{H}] \mathbf{N}^{\phi} \mathbf{N}^{\phi} \right\} \mathrm{d}\Omega, \end{aligned} \tag{11}$$

with **C** denoting tangent material matrix. More details on finite element formulation of the PF method, as CCPF algorithm can be found in [32].

3. Determination of Parameters of Elastoplasticity and Phase-Field for Monotonic Loading

3.1. Experimental Testing

As mentioned, the material considered is Astaloy™ Mo+0.2C of three densities, 6.5 g/cm^3, 6.8 g/cm^3 and 7.1 g/cm^3, manufactered by Höganäs AB [37]. The geometry of the testing samples is defined by ASTM E8 standard and it is given in [2].

The experimental testing was performed on 50 kN Instron servo-hydraulic testing machine. The machine is also equipped by GOM ARAMIS testing equipment (Carl Zeiss GOM Metrolog, Topomatika, Sveta Nedjelja, Croatia)consisting of video-extensometer. Additionally, testing is monitored by GOM® Aramis™ 12M digital image correlation (DIC) testing equipment.

Experiments with monotonic tensile loading were performed in Maribor at Faculty of Mechanical Engineering. All samples underwent strain-controlled loops at a rate of 1 mm/min. For each material density, seven test specimens have been evaluated. Figure 1a,b represents averaged results of the stress–strain and force-displacement curve obtained during tensile testing. The experiment is described in previous author's work [1] in more detail.

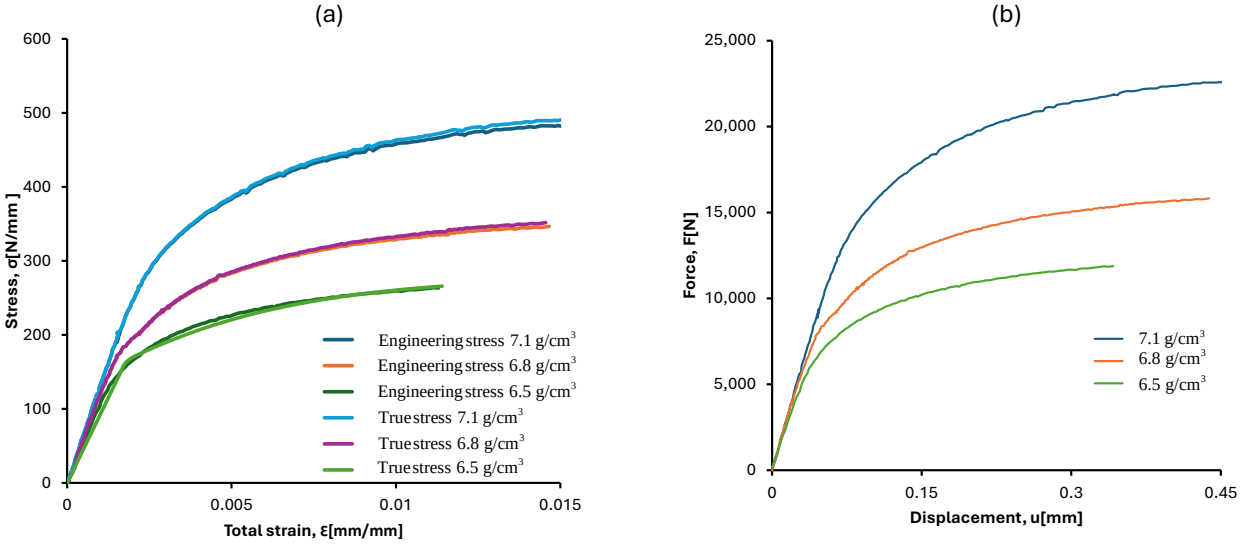

Figure 1. Stress–strain and force-displacement diagram of sintered steel Astaloy™ Mo+0.2C for densities 6.5 g/cm^3, 6.8 g/cm^3 and 7.1 g/cm^3: (**a**) stress–strain, (**b**) force-displacement.

As demonstrated by Figure 1 and discussed in [1], it can be seen that volume of porosity has significant impact on constitutive behaviour. The influence is less pronounced in the elastic range, but in the plastic range, the impact of the density is highly pronounced, which is in agreement with [38]. In the previous author's work, the elastoplastic material properties

of the microstructure constituents were determined in [39] by microindentation, where the macroscopic material parameters are determined from microscopic parameters. Unfortunately, the proposed models do not provide sufficiently accurate results of macroscopic material parameters within elastoplastic range. Furthermore, from comparison of true and engineering stress in Figure 1a, it can be concluded that small strain assumption is justified.

3.2. Numerical Validation

After experimental investigation, the next step is the calibration of the parameters required for numerical modelling. The geometry of the tensile test specimen is displayed in Figure 2, along with boundary conditions reflecting experimental setup. The loading of the specimen is imposed via displacement of the top surface, which improves stability of numerical simulations. In numerical modelling, 2D and 3D approaches have been evaluated. As known, PF methodology requires very dense mesh discretization. The two-dimensional model of the test specimen is discretized by 74,766 quadrilateral finite elements, while the three-dimensional model consists of 97,100 hexahedral finite elements. Mesh refinement is performed within expected fracture process zone (FPZ). In all simulations, length scale parameter required in PF has value $l = 0.3$ mm, which denotes minimum 2 finite elements appointed per thickness of the crack.

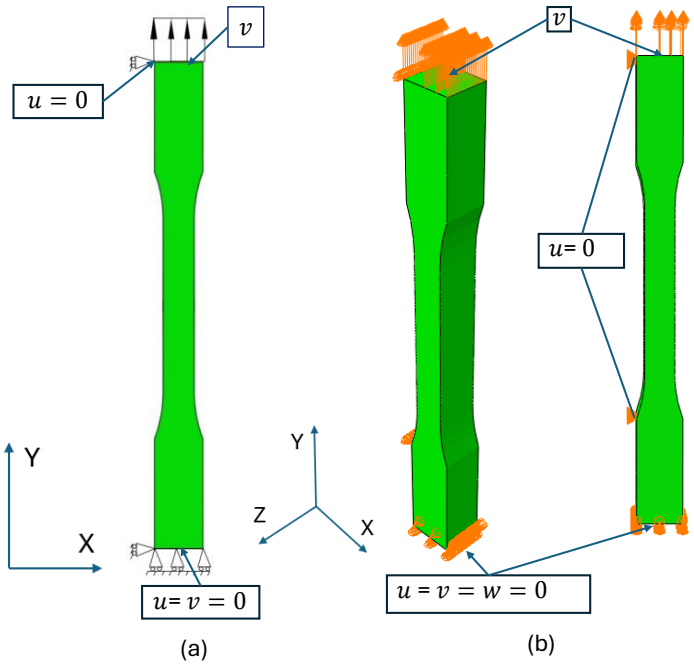

Figure 2. Numerical model of tensile test specimen with boundary conditions: (**a**) 2D, (**b**) 3D.

The parameters of elastoplastic behaviour are fitted by the least squares method, according to the constitutive laws in Equations (8) and (9). As known, the method operates by reducing the total discrepancies or differences between the known points and the fitted curve. The Levenberg–Marquardt algorithm was used for minimizing the approximation error, implemented in Python programming language. The calibrated elastoplastic material parameters for all densities are presented in Table 1.

Table 1. Parameters of elastoplastic behaviour.

Density	E [MPa]	ν [-]	σ_y^0 [MPa]	Q_∞ [MPa]	b [-]	γ_1 [-]	C_1 [MPa]
6.5 g/cm^3	98,000	0.28	165	50.9	315.313	253.162	14,802.035
6.8 g/cm^3	115,000	0.28	175	75	478.945	295.914	29,972.75
7.1 g/cm^3	131,000	0.28	265	102.7	395.036	306.46	36,714.587

Since damage in sinter steel initiates and propagates very suddenly, the threshold PF model has been chosen, where damage initiates at the moment of reaching energetic barrier ψ_c. The validity of this choice is supported by experimental testing conducted in [40], where several loading-unloading stages have been performed during tensile test. It has been demonstrated there is no change in the slope of the elastic domain. As mentioned before, the critical fracture energy ψ_c is determined as an area under the diagram obtained in Figure 1a. Critical strain energy values are presented in Table 2.

Table 2. Phase-field parameters.

Density	ψ_c [MPa]
6.5 g/cm^3	2.41
6.8 g/cm^3	3.85
7.1 g/cm^3	5.868

Moreover, in numerical modelling plane strain, as plane stress assumption has been assessed, along with 3D model. The comparison of the results obtained is displayed in Figure 3.

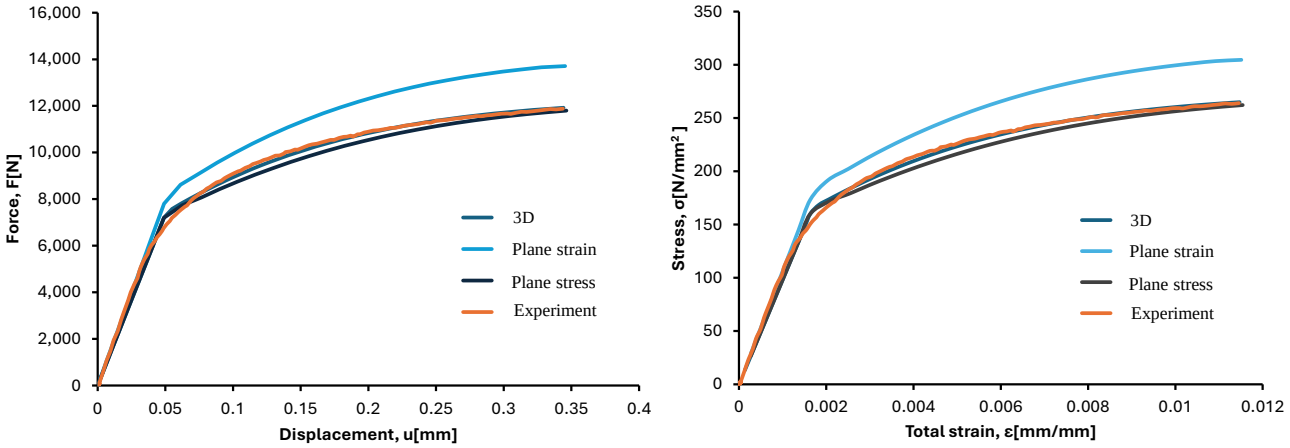

Figure 3. Comparison of numerical and experimental results of monotonic tensile test: (**a**) force-displacement diagram, (**b**) stress–strain diagram.

As can be seen, plane stress assumption and 3D model provide good correspondence to the experimental testing, while plane strain assumption overestimates force and stress. This is a consequence of the σ_z component appearing in plane strain state, especially at the onset of plastic yielding, as demonstrated in Figure 4.

Furthermore, in Figure 5, the comparison of experimentally and numerically obtained force-displacement and stress–strain diagrams for all three densities are displayed.

Furthermore, Figure 6 represents geometry of final crack obtained by numerical simulations, in 2D and 3D and comparison to the experimentally obtained fracture. The element deletion technique is used in simulations.

As can be concluded from Figure 6, the position of the final fracture obtained numerically is in very good agreement with the experimentally obtained results. Unfortunately, the orientation of the crack does not correspond. In the experiment, the orientation of the crack obeys brittle behaviour, while on the other hand, numerical simulations result in crack orientations obeying ductile damage. The reason for this discrepancy may lie in the distribution of porosities through the thickness of the specimen. In [40], metallographic images through the thickness of the specimen have been merged. There, it can be seen that the degree of porosity is much lower near the outside boundary of the specimen compared to the interior, where porosity is highly pronounced. This is a direct cosequence of the

production process. Since in numerical modelling material is taken as homogeneous, this assumption is obviously not in agreement with the real situation. Unfortunately, numerical modelling of varying material properties through the thickness of the specimen requires comprehensive metallographic investigation which is out of scope of this paper.

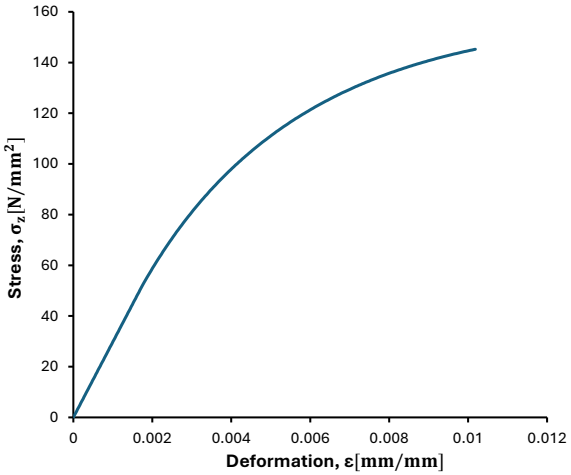

Figure 4. Change of σ_z component during monotonic tensile test for plane strain assumption.

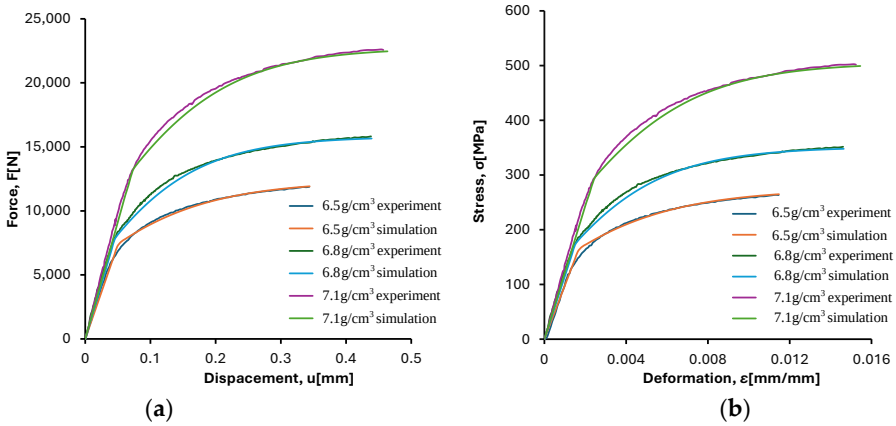

Figure 5. Comparison of experimentally and numerically obtained results of monotonic tensile test for all three densities: (**a**) force-displacement diagrams, (**b**) stress–strain diagrams.

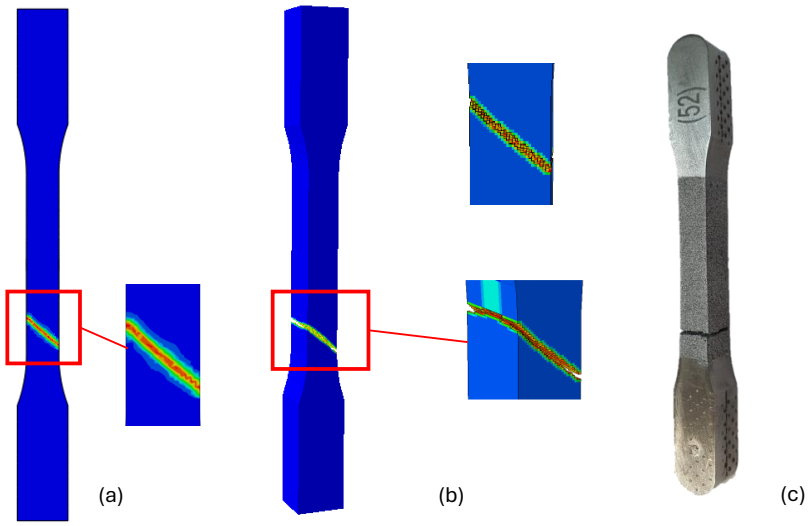

Figure 6. Comparison of the final fracture: (**a**) numerical 2D model, (**b**) numerical 3D model, (**c**) experiment.

4. Determination of Fatigue Phase-Field Parameters

In the following, fatigue behaviour of sintered steel is considered. The experimental tensile loading-unloading tests are provided on 50 kN frequency resonant machine Rumul, as described in previous research [40]. Cyclic loading is conducted at average frequency 130 Hz. Also, the loading ratio $R = 0.05$ is applied, presenting the ratio of maximum and minimum force within single cycle. The experiment is carried out on eleven specimens for all three densities, respectively. The experimentally obtained Wöhler curves in standard and logarithm form are presented on Figure 7a,b. It can be seen that the trend in the fatigue strength of the specimens is related to porosity (density of 6.5 g/cm^3 with highest porosity has the lowest fatigue strength compared to density of 7.1 g/cm^3 with the lowest porosity). The microscopic observation of all three different materials during fatigue and fracture is discussed in [40].

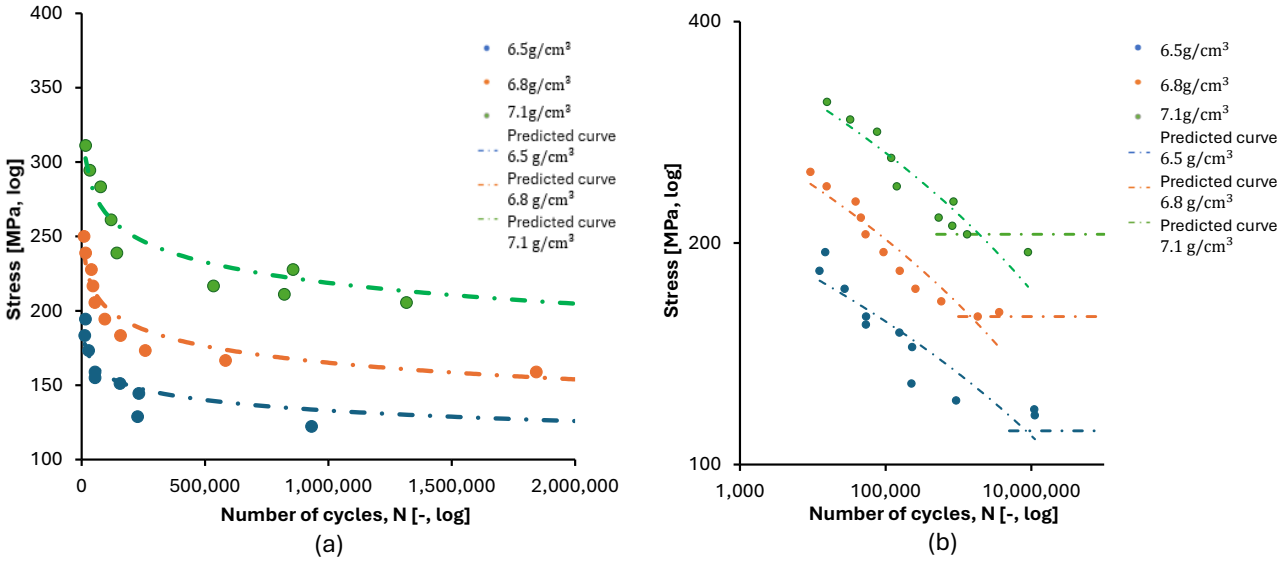

Figure 7. The comparison of stress-number of cycles curves: (**a**) standard and (**b**) logarithmic form.

4.1. Numerical Modelling of Fatigue Behaviour

Upon determining Wöhler's curves by experiments, the next step is their reconstruction by numerical simulations. In Section 2 is mentioned that for modelling of the fatigue and damage CCPF numerical algorithm provided in [32] is used. For modelling of fatigue, a 3D approach has been adopted. The key role in numerical modelling of fatigue is played by the fatigue degradation function, which consists of the accumulation variable and material dependant fatigue parameter ψ_∞. In this section, three degradation functions known from the literature [21] are utilized. Their efficiency in modelling of fatigue behaviour of sintered steel is expressed by comparison of coefficient of regression (R-squared) value. As explained before, the fatigue degradation function degrades energetic threshold ψ_c. Furthermore, it is known that numerical modelling of fatigue phenomena is time-consuming, especially for high-cycle fatigue (HCF). To alleviate this issue, the cycle skipping technique has been used, consisting of a two-step procedure to approximate the value of accumulation variable $\overline{\psi}$ [21]. The first step skips to the cycle when the initial degradation of the bulk material occurs, while the second step extrapolates the value of $\overline{\psi}$ after the onset of damage. The number of skipped cycles in the first step is given for all three degradation functions used:

$$\begin{aligned} N_1^{F_1} &= \frac{\overline{\psi}_\infty}{\Delta\overline{\psi}}\left(\sqrt{\frac{\psi_c}{\psi}-1}\right), \\ N_1^{F_2} &= \frac{\overline{\psi}_\infty}{\Delta\overline{\psi}}\left(1-\sqrt{\frac{\psi}{\psi_c}}\right), \\ N_1^{F_3} &= \frac{\overline{\psi}_\infty}{\Delta\overline{\psi}}10^{-\sqrt{\frac{\psi}{\psi_c}}} \end{aligned} \tag{12}$$

and it is determined after first loading cycle. To prevent any unwanted material degradation following cycle skipping, the number of skipped cycles according to Equation (12) is reduced for two cycles. The subsequent fatigue damage is predicted through application of the second step, utilizing the extrapolation technique outlined in [41] and adapted for the phase-field approach in [21]. The number of skipped and extrapolated cycles can be determined using the following relationship:

$$\Delta N_2 = q \frac{\Delta \overline{\psi}_1}{\Delta \overline{\psi}_1 - \Delta \overline{\psi}_2}, \tag{13}$$

based on two successive cycles demonstrating alterations in the accumulation variable $\Delta \overline{\psi}_1$ and $\Delta \overline{\psi}_2$, respectively. The parameter q denotes a parameter of fidelity, regulating the maximum value of permissible skipped cycles. The extrapolated value of accumulation variable is computed via relation:

$$\overline{\psi}(N + \Delta N_2) = \overline{\psi}(N) + \Delta \overline{\psi}_1 \Delta N_2 + \frac{1}{2}(\Delta \overline{\psi}_1 - \Delta \overline{\psi}_2)(\Delta N_2)^2. \tag{14}$$

More details on cycle skipping technique, as integration into CCPF algorithm is found in detail in [32], along with subroutines available for download. In this paper, the fidelity parameter is set as $q = 1$. To ensure that the number of extrapolated cycles does not overestimate the fatigue strength of the test specimen, considering the fast development of fatigue damage, the maximum value of ΔN_2 was limited to 20. Due to the quasi-brittle behaviour of sintered steel investigated in this paper, after the first occurrence of fatigue damage, final fatigue failure occurs very suddenly. Therefore, the first step of the cycle skipping provided a tremendous saving of computational time by jumping over most of the fatigue life of the test specimen. Since final fatigue failure occurs shortly after initiation, the second step of the cycle skipping has a small impact on the final numerical results.

Calibration of Fatigue Degradation Functions

Three fatigue degradation functions, presented in Section 2, are employed to encompass degradation of critical strain energy density ψ_c. Their performance has also been mutually compared for all densities. Based on the form of fatigue degradation functions, a constant value of parameter ψ_∞ should be sufficient for successful modelling of varying values of ψ_c, where the number of loading cycles upon failure obtained experimentally and numerically has been compared. Unfortunately, authors have not succeeded in calibration of ψ_∞ assuming its constant value. After finding ψ_∞ giving good correspondence to experimental results for one loading amplitude, its value gives significant error for other loading amplitudes. This error becomes even more prominent if ψ_∞ is calibrated on low-cycle fatigue (LCF) and afterwards evaluated on HCF or vice versa. The same behaviour has been experienced for all fatigue degradation functions assessed. Hence, it can be concluded that parameter ψ_∞ for sintered steel cannot preserve constant value. The other conclusion is that the fatigue degradation functions depending on a single fatigue parameter are not able to capture governing material degradation mechanisms as a consequence of fatigue. Therefore, authors have assumed that ψ_∞ is not constant for a specific material. A corelation of fatigue parameter ψ_∞ to the loading amplitude expressed through the maximum change in the elastic strain energy density $\Delta\psi_{max}$ is assumed $\psi_\infty = \psi_\infty(\Delta\psi_{max})$. The value of $\Delta\psi_{max}$ is taken after the first loading cycle as follows:

$$\Delta\psi_{max} = \int_0^1 \sigma d\varepsilon \tag{15}$$

By this, fatigue life of a component is expressed through the fatigue strength of the material point with the largest energy amplitude due to external loading. Despite the simple specimen geometry considered herein, the approach can be extended to complex geometry. Based on

the calibrated values of ψ_∞ for various loading amplitudes, their correlation is approximated by power function:

$$\psi_\infty = a(\Delta\psi_{\max})^b, \tag{16}$$

while a and b are material dependant coefficient and exponent, respectively, which are calibrated by least square method.

In Figure 8 are presented ψ_∞–$\Delta\psi_{\max}$ curves for all densities, obtained by fatigue degradation function F_1 (Equation (6)), while in Figures 9 and 10 are presented for functions F_2 and F_3, respectively. Table 2 represents the comparison of coefficients and exponents of power functions and R^2 parameters.

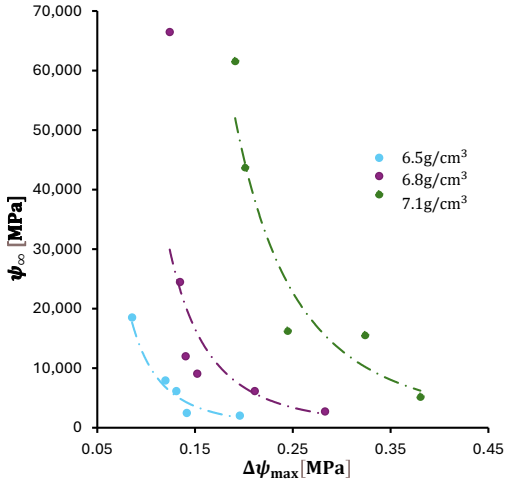

Figure 8. ψ_∞– $\Delta\psi_{\max}$ diagram for all material densities obtained by fatigue degradation function F_1.

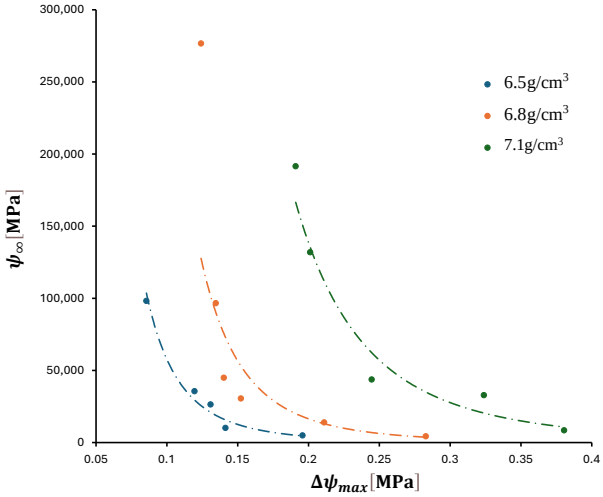

Figure 9. ψ_∞– $\Delta\psi_{\max}$ diagram for all material densities obtained by fatigue degradation function F_2.

From Table 3, it can be seen that the rising trend is present in the coefficients and exponents of power functions during decreasing porosity, which proves the physicality of the process. The exponent of the density 6.8 g/cm^3 does not match the trend, but also has the lowest R^2 parameter. On the other hand, for the other two densities of 6.5 and 7.1 g/cm^3, the power function as calibration curve shows great potential, where the R^2 parameter reaches values over 0.9. The comparison of the calibrated curves for all three densities is presented by R^2_{avg}. The F_3 degradation function shows the greatest value, which indicates it as the best option for describing the overall fatigue behaviour of sintered steel considered in this research. However, for specific densities, F_2 is the best option for 6.5 g/cm^3, F_3 is the best option for 6.8 g/cm^3 and F_2 is the best option for 7.1 g/cm^3.

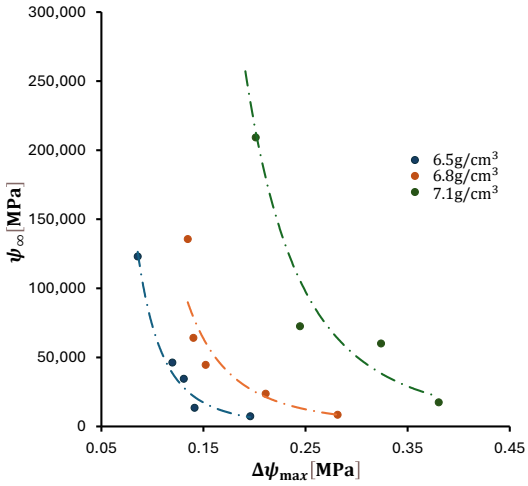

Figure 10. $\psi_\infty - \Delta\psi_{\max}$ diagram for all material densities obtained by fatigue degradation function F_3.

Table 3. Comparison and performance of the fitted parameters used for $\psi_\infty - \Delta\psi_{\max}$ diagrams.

Deg. Function		F_1			F_2			F_3	
Density [g/cm^3]	6.5	6.8	7.1	6.5	6.8	7.1	6.5	6.8	7.1
a	16.575	45.598	317.87	10.006	16.402	232.23	20.526	146.51	662.72
b	−2.836	−3.108	−3.079	−3.761	−4.294	−3.971	−3.55	−3.201	−3.601
R^2	0.9733	0.6585	0.927	0.9816	0.7483	0.96	0.9812	0.7704	0.9485
R^2_{avg}		0.8529			0.8966			0.90	

Also, in Figure 11 is presented the fatigue fracture on the test specimen obtained experimentally and in numerical simulation. In Figure 11a is displayed the distribution of the damage parameter ϕ at the onset of fracture, while in Figure 11b is displayed after fracture. From comparison of the fatigue fracture obtained by numerical model and experimental investigation, it can be seen that the shape of final fracture is approximately flat, which points to quasi-brittle fracture, with plasticity present on the microstructure.

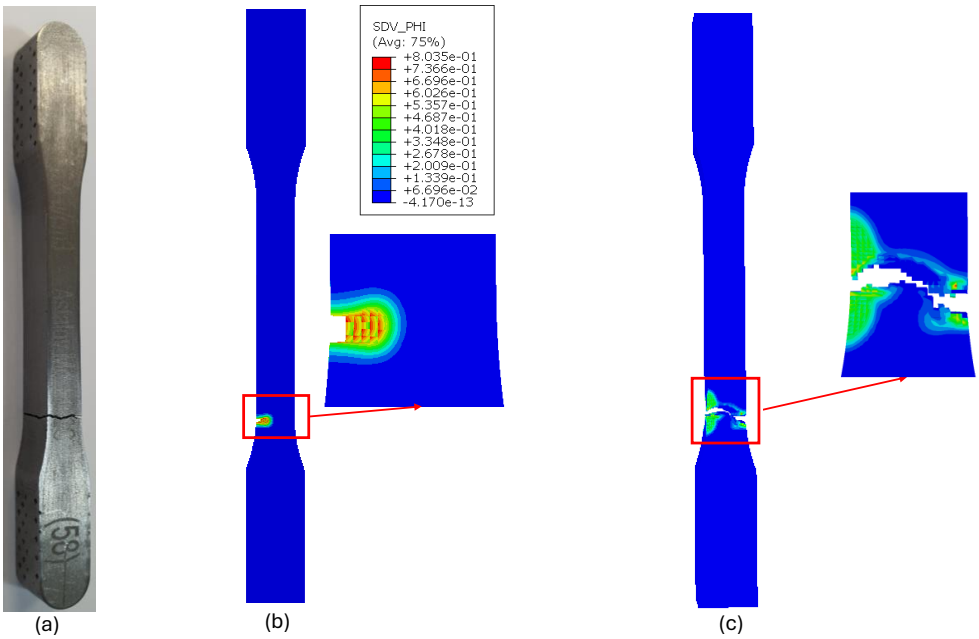

Figure 11. Fatigue fracture of test specimen: (**a**) experimental testing, (**b**) distribution of PF parameter at onset of damage and (**c**) after fracture.

5. Conclusions

In the paper, sintered steel Astaloy™ Mo+0.2C with three different densities, 6.5, 6.8 and 7.1 g/cm^3, is considered, manufactured by additive technology, exceedingly popular over the past decade. The purpose of this study is the calibration of the material and phase-field parameters on a macro scale based on the experiments conducted in monotonic and dynamic regime. From monotonic tensile tests, force-displacement, as stress–strain diagrams are obtained, while from the dynamically loaded specimens by the loading ratio $R = 0.05$, the Wöhler curves for all three densities are found.

For numerical modelling of proposed problems, a CCPF algorithm [32] is used with included cycle-skipping for reducing computational time during numerical simulations of fatigue. Based on the results of experiments provided in previous papers, material parameters are calibrated herein.

The elastoplastic material model used incorporates von Mises yield criterion, with combined nonlinear isotropic and kinematic hardening law. From the results of monotonic testing, material parameters of elastoplasticity and phase-field parameters (length scale parameter and the critical fracture energy) have been identified. For the test specimen geometry used in experiments, it has been concluded that plane strain assumption is not suitable for 2D modelling, due to disagreements in constitutive behaviour, as well as softening.

For modelling of fatigue, three fatigue degradation functions are utilized to calibrate Wöhler's curves for all considered densities. After initial calibration of single fatigue parameter ψ_∞, it has been concluded that one parameter with constant value is insufficient for appropriate modelling of fatigue. Therefore, ψ_∞ is related to the loading amplitude through maximum value of elastic strain energy density $\Delta\psi_{\max}$ after the first loading cycle. Their correlation in Wöhler's curves is expressed by power functions. The coefficients and the exponents of power function are calibrated by least square method. Based on the detailed comparison of fatigue degradation functions, it has been demonstrated that F_3 is generally the best option to capture fatigue of sintered steel for all densities considered. For specific densities, F_2 and F_3 capture Wöhler curves for specific densities.

Unfortunately, the authors are unable to conduct further experimental testing at the moment, which is essential for final confirmation of the calibrated fatigue parameters and correlation of ψ_∞ and $\Delta\psi_{\max}$. Therefore, the plan for future research includes experimental testing on specimens of more complex geometry with nonhomogeneous stress distribution.

Author Contributions: Writing—original draft preparation, T.P.; writing—review and editing, T.L.; supervision, Z.T. All authors have read and agreed to the published version of the manuscript.

Funding: This research received no external funding.

Data Availability Statement: The original contributions presented in the study are included in the article, further inquiries can be directed to the corresponding author.

Conflicts of Interest: The authors declare no conflicts of interest.

References

1. Tomić, Z.; Gubeljak, N.; Jarak, T.; Polančec, T.; Tonković, Z. Micro- and macromechanical properties of sintered steel with different porosity. *Scr. Mater.* **2022**, *217*, 114787. [CrossRef]
2. Polančec, T.; Lesičar, T.; Rako, J. Constitutive Modelling of Sintered Steel by Phase-field Method. *Struct. Integr. Procedia* **2023**, *52*, 348–355. [CrossRef]
3. Hakim, V.; Karma, A. Laws of crack motion and phase-field models of fracture. *J. Mech. Phys. Solids* **2008**, *57*, 342–368. [CrossRef]
4. Griffith, A.A.; Taylor, G.I. VI. The phenomena of rupture and flow in solids: Containing Papers of a Mathematical or Physical Character. *Philos. Trans. R. Soc. Lond. Ser. A* **1921**, *221*, 163–198. [CrossRef]
5. Francfort, G.A.; Marigo, J.J. Revisiting brittle fracture as an energy minimization problem. *J. Mech. Phys. Solids* **1998**, *46*, 1319–1342. [CrossRef]
6. Bourdin, B.; Francfort, G.A.; Marigo, J.-J. Numerical experiments in revisited brittle fracture. *J. Mech. Phys. Solids* **2000**, *48*, 797–826. [CrossRef]

7. Miehe, C.; Hofacker, M.; Welschinger, F. A phase field model for rate-independent crack propagation: Robust algorithmic implementation based on operator splits. *Comput. Methods Appl. Mech. Eng.* **2010**, *199*, 2765–2778. [CrossRef]
8. Ambati, M.; Gerasimov, T.; De Lorenzis, L. A review on phase-field models of brittle fracture and a new fast hybrid formulation. *Comput. Mech.* **2015**, *55*, 383–405. [CrossRef]
9. De Lorenzis, L.; Gerasimov, T. Numerical implementation of phase-field models of brittle fracture BT. In *Modeling in Engineering Using Innovative Numerical Methods for Solids and Fluids*; De Lorenzis, L., Düster, A., Eds.; CISM International Centre for Mechanical Sciences: Udine, Italy; Springer International Publishing: Cham, Switzerland, 2020; Volume 599, pp. 75–101. [CrossRef]
10. Seleš, K.; Lesičar, T.; Tonković, Z.; Sorić, J. A residual control staggered solution scheme for the phase-field modeling of brittle fracture. *Eng. Fract. Mech.* **2019**, *205*, 370–386. [CrossRef]
11. Aldakheel, F.; Schreiber, C.; Müller, R.; Wriggers, P. *Phase-Field Modeling of Fatigue Crack Propagation in Brittle Materials: Current Trends and Open Problems in Computational Mechanics*; Springer Nature: Berlin/Heidelberg, Germany, 2022; p. 15.
12. Ambati, M.; Gerasimov, T.; De Lorenzis, L. Phase-field modeling of ductile fracture. *Comput. Mech.* **2015**, *55*, 1017–1040. [CrossRef]
13. Yin, B.; Kaliske, M. A ductile phase-field model based on degrading the fracture toughness: Theory and implementation at small strain. *Comput. Methods Appl. Mech. Eng.* **2020**, *366*, 113068. [CrossRef]
14. Levitas, V.I.; Warren, J.A. Phase field approach with anisotropic interface energy and interface stresses: Large strain formulation. *J. Mech. Phys. Solids* **2016**, *91*, 94–125. [CrossRef]
15. Amendola, G.; Fabrizio, M.; Golden, J.M. Thermomechanics of damage and fatigue by a phase field model. *J. Therm. Stress.* **2016**, *39*, 487–499. [CrossRef]
16. Caputo, M.; Fabrizio, M. Damage and fatigue described by a fractional derivative model. *J. Comput. Phys.* **2015**, *293*, 400–408. [CrossRef]
17. Carrara, P.; Ambati, M.; Alessi, R.; De Lorenzis, L. A framework to model the fatigue behavior of brittle materials based on a variational phase-field approach. *Comput. Methods Appl. Mech. Eng.* **2020**, *361*, 112731. [CrossRef]
18. Alessi, R.; Vidoli, S.; De Lorenzis, L. A phenomenological approach to fatigue with a variational phase-field model: The one-dimensional case. *Eng. Fract. Mech.* **2018**, *190*, 53–73. [CrossRef]
19. Seiler, M.; Linse, T.; Hantschke, P.; Kästner, M. An efficient phase-field model for fatigue fracture in ductile materials. *Eng. Fract. Mech.* **2020**, *224*, 106807. [CrossRef]
20. Ulloa, J.; Wambacq, J.; Alessi, R.; Degrande, G.; François, S. Phase-field modeling of fatigue coupled to cyclic plasticity in an energetic formulation. *Comput. Methods Appl. Mech. Eng.* **2021**, *373*, 113473. [CrossRef]
21. Seleš, K.; Aldakheel, F.; Tonković, Z.; Sorić, J.; Wriggers, P. A general phase-field model for fatigue failure in brittle and ductile solids. *Comput. Mech.* **2021**, *67*, 1431–1452. [CrossRef]
22. Khalil, Z.; Elghazouli, A.Y.; Martínez-Pañeda, E. A generalised phase field model for fatigue crack growth in elastic–plastic solids with an efficient monolithic solver. *Comput. Methods Appl. Mech. Eng.* **2022**, *388*, 114286. [CrossRef]
23. Bourdin, B.; Francfort, G.A.; Marigo, J.-J. The Variational Approach to Fracture. *J. Elast.* **2008**, *91*, 5–148. [CrossRef]
24. Duda, F.P.; Ciarbonetti, Á.A.; Sánchez, P.J.; Huespe, A.E. A phase-field/gradient damage model for brittle fracture in elastic–plastic solids. *Int. J. Plast.* **2015**, *65*, 269–296. [CrossRef]
25. Wick, T. Modified Newton methods for solving fully monolithic phase-field quasi-static brittle fracture propagation. *Comput. Methods Appl. Mech. Eng.* **2017**, *325*, 577–611. [CrossRef]
26. Farrell, P.E.; Maurini, C. Linear and nonlinear solvers for variational phase-field models of brittle fracture. *Int. J. Numer. Methods Eng.* **2015**, *109*, 648–667. [CrossRef]
27. Ambati, M.; Kruse, R.; De Lorenzis, L. A phase-field model for ductile fracture at finite strains and its experimental verification. *Comput. Mech.* **2016**, *57*, 149–167. [CrossRef]
28. Nagaraja, S.; Carrara, P.; De Lorenzis, L. Experimental characterization and phase-field modeling of anisotropic brittle fracture in silicon. *Eng. Fract. Mech.* **2023**, *293*, 109535. [CrossRef]
29. Mattey, R.; Jewell, B.; Ghosh, S.; Sain, T. Phase-field fracture coupled elasto-plastic constitutive model for 3D printed thermoplastics and composites. *Eng. Fract. Mech.* **2023**, *291*, 109535. [CrossRef]
30. Hug, L.; Dahan, G.; Kollmannsberger, S.; Rank, E.; Yosibash, Z. Predicting Fracture in the Proximal Humerus using Phase Field Models. *J. Mech. Behav. Biomed. Mater.* **2022**, *134*, 105415. [CrossRef]
31. Haveroth, G.A.; Garcia, M.; Vale, D.; Bittencourt, M.L.; Boldrini, J.L.; Haveroth, G.A. A Non-isothermal Thermodynamically Consistent Phase Field Model for Damage, Fracture and Fatigue Evolutions in Elasto-Plastic Materials. *Comput. Methods Appl. Mech. Eng.* **2020**, *364*, 112962. [CrossRef]
32. Lesičar, T.; Polančec, T.; Tonković, Z. Convergence-Check Phase Field Scheme for Modelling of Brittle and Ductile Fracture. *Submit. Eng. Fract. Mech.* **2023**, *13*, 7776. [CrossRef]
33. Amor, H.; Marigo, J.J.; Maurini, C. Regularized formulation of the variational brittle fracture with unilateral contact: Numerical experiments. *J. Mech. Phys. Solids* **2009**, *57*, 1209–1229. [CrossRef]
34. Freddi, F.; Royer-Carfagni, G. Regularized variational theories of fracture: A unified approach. *J. Mech. Phys. Solids* **2010**, *58*, 1154–1174. [CrossRef]
35. Chaboche, J.L. Constitutive equations for cyclic plasticity and cyclic viscoplasticity. *Int. J. Plast.* **1989**, *5*, 247–302. [CrossRef]
36. Dassault Systemes Simulia Corporation. *Abaqus/Standard 6.14*; Dassault Systemes Simulia Corporation: Providence, RI, USA, 2014.
37. Höganäs AB. *Hipaloy® Product Brochures*; Höganäs AB: Höganäs, Sweden, 2011.

38. Chawla, N.; Deng, X. Microstructure and mechanical behavior of porous sintered steels. *Mater. Sci. Eng. A* **2004**, *390*, 98–112. [CrossRef]
39. Tomić, Z.; Jarak, T.; Pavlović, B.; Tonković, Z. On Extracting Stress–Strain Curves of Porous Multi-Phase Sintered Steels by Microindentation. *Exp. Tech.* **2023**, *48*, 657–675. [CrossRef]
40. Tomić, Z.; Jarak, T.; Lesičar, T.; Gubeljak, N.; Tonković, Z. Modelling of Fatigue Microfracture in Porous Sintered Steel Using a Phase-Field Method. *Materials* **2023**, *16*, 4174. [CrossRef]
41. Cojocaru, D.; Karlsson, A. A simple numerical method of cycle jumps for cyclically loaded structures. *Int. J. Fatigue* **2006**, *28*, 1677–1689. [CrossRef]

Disclaimer/Publisher's Note: The statements, opinions and data contained in all publications are solely those of the individual author(s) and contributor(s) and not of MDPI and/or the editor(s). MDPI and/or the editor(s) disclaim responsibility for any injury to people or property resulting from any ideas, methods, instructions or products referred to in the content.